AKADÉMIAI KIADÓ

UNIVERSITY of DEBRECEN

International Review of Applied Sciences and Engineering

13 (2022) 3, 309–320

DOI:
10.1556/1848.2021.00389

ORIGINAL RESEARCH PAPER

Force-displacement relationships for NiTi alloy helical springs by using ANSYS: Superelasticity and shape memory effect

Chayma El Mtili[1]*, Abdellatif Khamlichi[1],
Loubna Hessissen[1] and Hafiz Muhammad Waqas Badar[2]

[1] Systems of Communications and Detection Laboratory, University Abdelmalek Essaadi, 93030, Tetouan, Morocco

[2] Al-Khawarzmi Institute of Computer Science, University of Engineering and Technology Lahore, Pakistan

Received: September 26, 2021 • Accepted: November 17, 2021

ABSTRACT

Shape memory alloys are smart materials which have remarkable properties that promoted their use in a large variety of innovative applications. In this work, the shape memory effect and superelastic behavior of nickel-titanium helical spring was studied based on the finite element method. The three-dimensional constitutive model proposed by Auricchio has been used through the built-in library of ANSYS® Workbench 2020 R2 to simulate the superelastic effect and one-way shape memory effect which are exhibited by nickel-titanium alloy. Considering the first effect, the associated force-displacement curves were calculated as function of displacement amplitude. The influence of changing isothermal body temperature on the loading-unloading hysteretic response was studied. Convergence of the numerical model was assessed by comparison with experimental data taken from the literature. For the second effect, force-displacement curves that are associated to a complete one-way thermomechanical cycle were evaluated for different configurations of helical springs. Explicit correlations that can be applied for the purpose of helical spring's design were derived.

KEYWORDS

shape memory alloys, helical spring, finite element analysis, thermomechanical loading, superelasticity, shape memory effect, ANSYS

1. INTRODUCTION

Shape Memory Alloys (SMA) have attracted much attention for the last few decades due to their excellent mechanical properties as well as their essential aspects of deformation and transformation in structural behavior [1, 2]. Recent increase in applications of these materials in a wide variety of fields, such as aerospace, medical, civil and mechanical engineering, has led to an increased focus on modeling their thermomechanical response. SMA materials exhibit two significant macroscopic phenomena which are called the SuperElasticity (SE) and Shape Memory Effect (SME) [3]. Both these effects are used in practice in order to design devices that enable achieving special functions. In many engineering applications, SMA helical springs are used as actuator devices. This structure is considered in the actual work in order to derive, through numerical simulations by means of ANSYS® Workbench 2020 R2, force-displacement relationships that can be used to carry out smart design of these devices.

Various SMA materials were discovered since they were first revealed in the thirties of the last century. They can be differentiated according to their thermomechanical characteristics, as well as working range of temperature and cost. Among them, the nickel-titanium alloy (NiTi or Nitinol) has gained substantial interest in practice. This may be explained by its

*Corresponding author. Tel.: +212-652-843-289.
E-mail: elmtili.h@gmail.com

AKJournals

significant advantages over the other families of SMA, such as stable transformation temperatures, effective thermal memory, high corrosion resistance, high mechanical performances and the faculty of undergoing large deformation [1]. Stable transformation temperatures means here that transformation profiles during cooling, following thermal cycling for heat treatment purpose, tend to stabilize after performing a sufficient number of cycles. It is then possible to reach transformation temperatures which are almost independent from the number of work cycles if the range of temperatures is consistent with heat treatment [4]. The NiTi SMA alloy shows in practice a high quality-price ratio. It was discovered in the 1960s, at the Naval Ordnance Laboratory [5], and it is considered to be a superelastic material with recoverable memory strains of up to 8% [6]. This SMA material is selected as the design material of helical springs considered in the present study.

To simulate SMA response, the finite element method is used under ANSYS software. Considering the SE effect, use is made of the constitutive model proposed first by Auricchio et al. [5] and improved later by Auricchio and Taylor [7] in order to capture the asymmetrical behavior of SMA during a tension-compression test. The material option for the SME effect is based on the 3D thermomechanical constitutive equations for solid phase transformations induced by stresses as proposed by Auricchio and Petrini [8], Auricchio [9] and Souza et al. [10]. These models have been recognized to yield suitable results for common SMA applications. Both of these models have been successfully implemented into the finite element based commercial software ANSYS [3, 11]. It should be mentioned that to date ANSYS code is the only software able to implement both SE and SME without needing special development of user material subroutines [12]. These two options can be accessed directly via the Temperature Bulk (TB) – SMA command of ANSYS.

Use is made in the following of ANSYS simulation environment in order to assess in closed form force-displacement relationships for various configurations of helical springs, under both SE and SME situations. The aim is to present an alternative way to existing analytical approaches that can be employed to ease the design procedure of arbitrary SMA applications that are based on helical springs. This is because existing analytical models suffer in general from the shortcoming that their accuracy depends largely on the actual geometric configuration of the structure and the loading applied to it [13, 14]. On the opposite, numerical simulations can be carried out parametrically in order to derive useful correlations that provide direct handling of the design procedure in the framework of special helical spring's applications [15].

Considering the SE effect, the force-displacement curves are calculated as function of displacement amplitude and body isothermal temperature. Convergence of the finite element model will be assessed through comparison of the obtained numerical predictions with experimental data taken from the literature. In contrast to the SE effect, the SME effect has been rarely studied in literature. Considering the one-way MSE effect, the reaction force curve needed to reach a desired course of a given helical spring will be evaluated for different configurations including various values of wire radius, coil radius and initial length.

2. MATERIALS AND METHODS

2.1. Numerical simulations performed on SMA NiTi alloy

SMA alloys show diverse shape-memory effects. Two common encountered effects are: superelasticity or pseudoelasticity, and one-way shape memory. The first effect SE designates the capability of recovering the original shape after undergoing large deformations that are induced by pure mechanical loading, see Fig. 1.

The second effect which is termed SME indicates the ability to recover the original shape by simple heating (above austenite finish temperature) after being initially mechanically deformed at a sufficiently low temperature. Figure 2 presents the thermomechanical trajectory associated to a one-way SME. This effect is used in many applications of SMA where self expanding of a part under the effect of temperature is required. Deployment is performed in general at room temperature for which the part is initially stressed to deform it plastically and then unloaded to get a permanent strained shape. Then, temperature is increased up to finish temperature of the austenitic transformation to yield countersense deformation. This enables to get back the initial shape which results to be insensitive to temperature. In practice, the CDA branch of Fig. 2 is used by special monitoring of body temperature.

It should be noticed that a two-way effect is also encountered in SMA, but it needs special training of the material and is discarded in the actual study.

In the current work, three-dimensional finite element analysis was used to perform simulation of helical springs

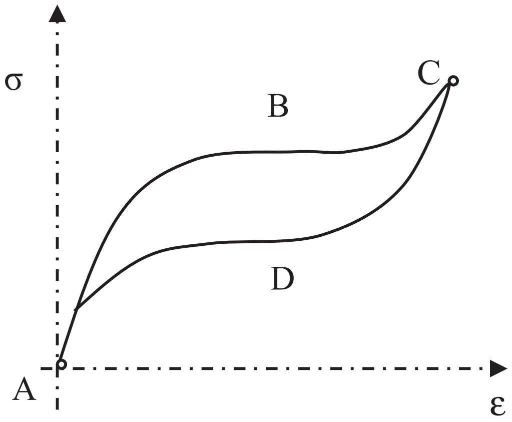

Fig. 1. Superelasticity effect: at constant high temperature the material is first loaded (ABC), it shows a nonlinear behavior, while during unloading (CDA) the reverse transformation occurs forming a flag-shape hysteresis

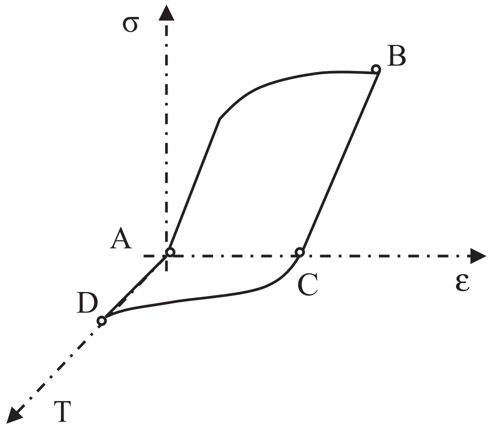

Fig. 2. One-way shape memory effect: at the end of a mechanical loading-unloading path (ABC) performed at constant low temperature, the material presents residual deformation (AC), the residual strain may be recovered through a thermal cycle (CDA)

undergoing static deformation when subjected to the action of a thermomechanical loading, for both SE and SME effects scenarios. Simulation was performed by using the commercial software ANSYS® Workbench 2020 R2. This was carried out through the ANSYS CAE interface [16]. Finite strains were automatically integrated in the analysis.

The importance of numerical simulation in the case of SMA NiTi helical springs is that it enables to predict the system response, under arbitrary situations regarding either SE or SME effect. The deformation undergone by the particular structure of a helical spring is completely three-dimensional and cannot be rendered satisfactorily through simplified analytical modeling. Given a spring section, partial transformation occurs between martensite and austenite phases during deformation and one-dimensional based approaches fail to capture this phenomenon. The constitutive equations used in simulation of helical springs made of Nitinol alloy are based on the SMA Auricchio model which is implemented in the ANSYS finite element code [17, 18]. Two major features make this modeling quite useful and appropriate [19]. First of all, the number of constitutive parameters used during the analysis is reduced to a strict minimum; so they can be accurately identified experimentally. Secondly, it is unnecessary to utilize a USER Material Subroutine (USERMAT), since the model is implemented by default in the 2020 R2 version of ANSYS software, which we have used in this work, and can then be directly accessed through the Temperature Bulk (TB) command.

Explicit equations of the SMA Auricchio based material model, which was chosen here to describe the coupled thermomechanical behavior of NiTi, are recalled in Appendixes A and B.

2.2. Material properties of NiTi SMA alloy used in simulations

2.2.1. Material properties for SE effect. The SMA helical springs material properties used here correspond to the experimental data given by Huang et al. [20]. The numerical simulations under ANSYS that are associated to the SE effect were performed by using material parameters that were calculated at the reference temperature $T = 25°C$. They are listed in Table 1.

The values of temperature parameters given in Table 1 were calculated by using the following linearized formulas, [20], which hold for ambient temperature that verifies $T \geq M_s$:

$$\sigma_{Af} = C_A\left(T - A_f\right) \tag{1}$$

$$\sigma_{As} = C_A(T - A_s) \tag{2}$$

$$\sigma_{Ms} = \sigma_s + C_M(T - M_s) \tag{3}$$

$$\sigma_{Mf} = \sigma_f + C_M(T - M_s) \tag{4}$$

where σ_{Ms} and σ_{Mf} are respectively the critical stresses at the beginning and end of the martensitic transformation, σ_{As} and σ_{Af} are respectively the critical stresses at the beginning and end of the austenitic transformation, and σ_s and σ_f are respectively the critical uniaxial start and finish stresses, while the SMA material transforms from twinned martensite to detwinned martensite. The material parameters related to the martensite and austenite phases are denoted respectively C_M and C_A. M_s is temperature at the beginning of the martensitic transformation. A_s and A_f are respectively the temperatures at the beginning and end of the austenitic transformation.

As ANSYS admits only a single Young's modulus, an average value elastic modulus E was calculated by using the austenite and martensite Young's moduli [21]. The obtained average value $E = 68$ GPa enables to get a closer agreement with the experimental curves.

Table 1. Material properties of the NiTi SMA helical springs used for the simulation of SE effect

Parameter	Value
σ_s	96 MPa
σ_f	582 MPa
Maximum residual shear stain ε_L	0.032 $m.m^{-1}$
C_A	11 $MPa.K^{-1}$
C_M	7.6 $MPa.K^{-1}$
Austenite Young modulus E_A	72 GPa
Martensite Young modulus E_M	64 GPa
Overage Young's modulus $E = (E_A + E_M)/2$	68 GPa
Poisson's ratio ν	0.33
Material parameter α	0.15
Reference temperature T	25°C
Temperature M_s	268 K
Temperature M_f	268 K
Temperature A_s	278 K
Temperature A_f	288 K
σ_{Af}	111.6 MPa
σ_{As}	221.6 MPa
σ_{Ms}	325.1 MPa
σ_{Mf}	811.1 MPa

On the other hand, to use Auricchio model one needs to enter the material parameter α that operates the scaling of compression response from that of tension response. Since this parameter was not evaluated experimentally in [20], it was treated as a parameter to be identified in order to get the closest match between simulated results and experimental curves. It was found that $\alpha = 0.15$ achieves the best fit.

2.2.2. Material properties for SME effect. To perform simulation of the SME effect by means of ANSYS software, material parameters that are needed as inputs were those given in [22]. Taking the reference temperature to be $T = 23°C$, the parameters needed for simulation of SME effect for NiTi SMA material are presented in Table 2.

2.3. Geometry of the SMA helical springs used in simulations

2.3.1. Geometry of the helical spring used for SE effect. Huang et al. [20] have considered four different geometries of helical springs and studied their response during a tensile test experiment. In this work, focus is on the helical spring denoted SMA (b) in that reference and for which the geometric parameters are given in Table 3.

2.3.2. Geometry of the helical springs used for SME effect. Nine different geometries of helical springs have been considered in order to assess dependency of the load-displacement curve on the actual geometry of the helical spring. All the helical springs have the same number of coils which was fixed at $N = 7$, and the same wire radius which was fixed at $r_0 = 0.4\ mm$. A full factorial design of experiment table was then constructed by choosing three levels of coil radius and initial length. Table 4 recalls all the possible combinations of geometric parameters that are used in this work. The initial pitch angle of a spring was computed according to the following equation [20]:

$$\alpha_0 = \tan^{-1}\left(\frac{L_0}{2\pi R_0 N}\right) \tag{5}$$

Table 2. Material properties of NiTi helical springs used for the analysis of SME effect

Parameter	Value
Hardening parameter h	$500\ MPa$
Reference temperature	23°C
Elastic limit R	$120\ MPa$
Temperature scaling parameter β	$8.3\ MPa.°C^{-1}$
Lode dependency parameter m	0
Maximum transformation stain ε_L	$0.07\ m.m^{-1}$
Martensite Young modulus E_M	$70\ GPa$
Young's modulus E	$60\ GPa$
Poisson's ratio ν	0.33

Table 3. Geometric parameters of the NiTi helical spring used in SE effect simulations

Coil radius R_0 (mm)	Wire radius r_0 (mm)	Initial length L_0 (mm)	Number of coils N
6.1	0.4	19	7

Table 4. Geometric parameters of NiTi helical springs used in SME effect simulations

Specimen identification	Coil radius R_0 (mm)	Initial length L_0 (mm)	Initial pitch angle α_0 (°)
SMA (1)	5.1	17	4.334
SMA (2)	5.1	19	4.842
SMA (3)	5.1	21	5.348
SMA (4)	5.4	17	4.094
SMA (5)	5.4	19	4.574
SMA (6)	5.4	21	5.053
SMA (7)	5.7	17	3.879
SMA (8)	5.7	19	4.334
SMA (9)	5.7	21	4.788

2.4. Boundary conditions and thermomechanical loads

2.4.1. Helical spring for SE effect. The helical spring is assumed to be anchored at its left extremity, while at its right extremity it is subjected to a prescribed loading-unloading cycle of displacement which is applied in the spring's longitudinal direction with a given amplitude. Body helical spring temperature is assumed to be uniform. The considered mechanical displacement amplitude and body isothermal temperature were fixed by choosing three levels for each factor. Table 5 gives the resulting 9 combinations constructed on these variables. Figure 3 gives the profile of applied displacement.

2.4.2. Helical springs for one-way SME effect. Helical springs considered here are assumed to be clamped at their left extremity. Their right extremity is subjected to a prescribed displacement, while body temperature, which is assumed to be uniform, is varied. The 3D Auricchio model of the Ni-Ti helical spring was used to simulate SME in ANSYS Workbench platform, through the static structural

Table 5. Combinations of thermomechanical loading prescribed to the helical spring

Combination number	Displacement amplitude U (m)	Isothermal temperature T $(°C)$
1	0.06	15
2	0.06	25
3	0.06	35
4	0.08	15
5	0.08	25
6	0.08	35
7	0.1	15
8	0.1	25
9	0.1	35

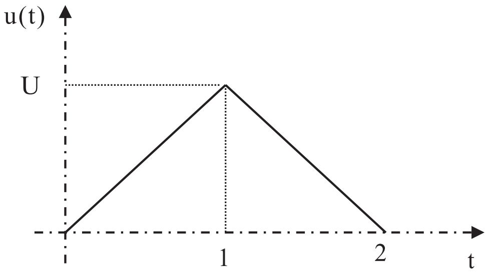

Fig. 3. Applied displacement at the right extremity of helical spring for SE analysis; U is the amplitude of displacement while $u(t)$ is the instantaneous value of displacement at chronological time t

module according to the material properties which are given in Table 2.

The SME simulation was carried out through applying a combination of thermal and mechanical loading. The simulation was done based on five steps that are illustrated in Fig. 4. At the first step, the material body temperature was decreased from the reference temperature of 23°C to the lower temperature of 5°C. This thermal loading is applied in order to get the reverse transformation of the material from the austenite phase zone $(A_f \leq T)$, which corresponds to the actual reference temperature of 23°C, toward the twinned martensite phase $(T \leq M_f)$ for the lower temperature of 5°C. To calculate the solution during this step, ANSYS software uses the 3D thermomechanical constitutive equations that are derived from Auricchio and Petrini model [8], as given in Appendix B.

During the second step, the temperature of the spring was fixed at 5°C and a compression displacement of -35 mm was applied. This was followed in the third step by unloading the helical spring to reach zero displacement state, at the same body temperature of 5°C. In the fourth step, the body temperature of the load free spring was increased to reach 100°C, so the material was transformed to the austenite phase to fully recover the deformation. Finally, at the fifth step the material body temperature was decreased to reach again 5°C. This achieves the complete one-way SME cycle.

In order to ensure convergence of the nonlinear procedure, each step consisted of a minimum of 400 sub-steps.

2.5. Finite element mesh used in simulations

The finite element analysis (FEA) was carried out in ANSYS$^®$ Workbench 2020 R2 by generating a three-dimensional solid model for each considered geometry of SMA helical springs. For both SE and SME simulations, mesh generation was made by using 3D structural elements of type SOLID186 and by selecting the tetrahedrons method of meshing. Mesh convergence was assessed by reducing the size of elements until asymptotic stability of solution is reached. The total number of elements used for meshing any of the considered helical spring's domains was then fixed at 1,693, and the associated number of nodes is 4,831.

3. RESULTS AND DISCUSSION

3.1. Simulation of SE effect in SMA helical springs

3.1.1. Convergence of the ANSYS modeling. Simulations were conducted for the SMA helical spring made of NiTi having the material properties given in Table 1 and for which the geometry parameters are those given in Table 3. The considered thermomechanical loading conditions, consisting of uniform body temperature fixed at 25°C and prescribed cycle of displacement with positive amplitude at the right extremity of helical spring, were fixed according to lines 2, 5 and 8 of Table 5.

Figure 5 depicts the 3D geometry of SMA helical spring elaborated under ANSYS CAE interface.

Figure 6 gives the converged mesh used in all simulations.

Figure 7 shows the boundary conditions that are prescribed to the SMA helical spring.

To get an interesting behavior of the SMA helical spring in terms of SE effect, finite deformation is needed. This is why the amplitude of applied displacement was chosen to be large enough. For instance, applying the maximum displacement of 100 mm represents more than five times the initial length of helical springs. Figure 8 shows the SMA helical spring in initial and deformed configurations.

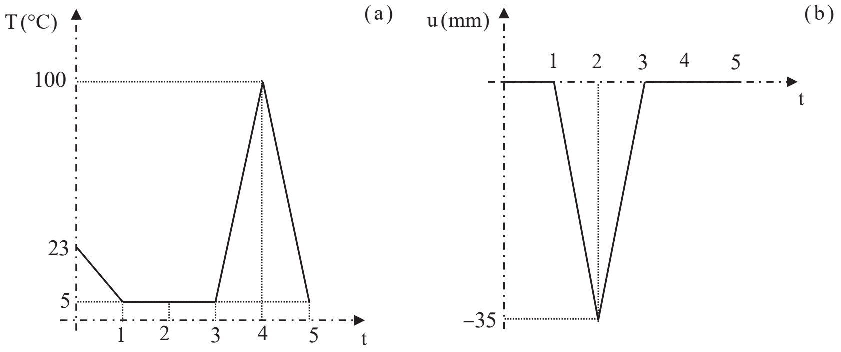

Fig. 4. SME analysis; applied body isothermal temperature (a) and displacement at the right extremity of helical springs (b)

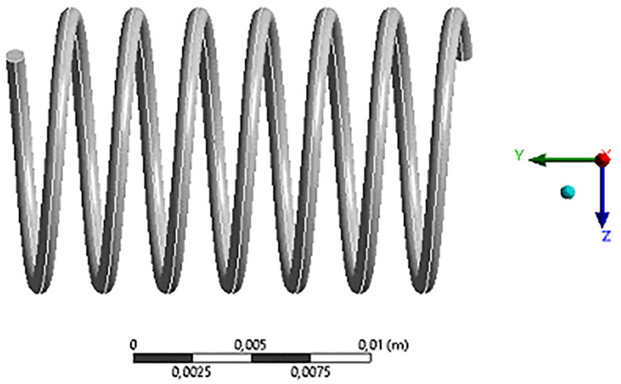

Fig. 5. Geometry of the SMA helical spring part considered for the analysis of SE effect

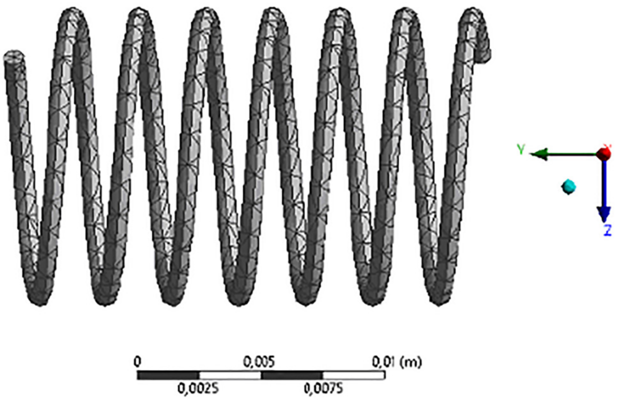

Fig. 6. Mesh for the SMA helical spring considered for the analysis de SE effect

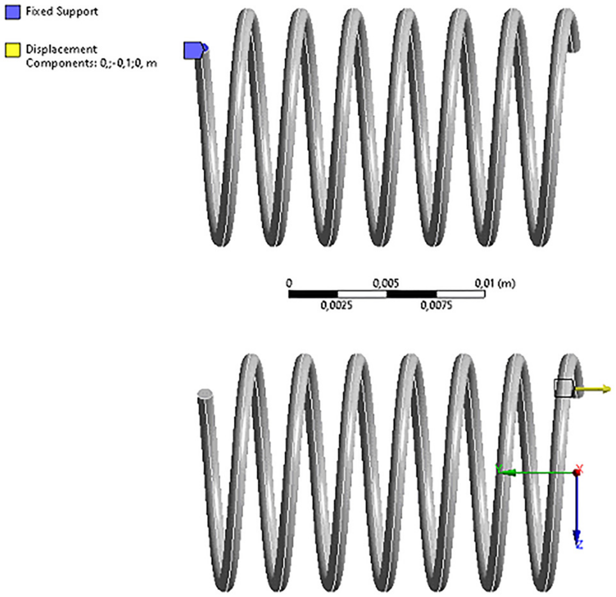

Fig. 7. Boundary conditions applied to the NiTi SMA helical spring

To assess convergence of the modeling under ANSYS software, Fig. 9 shows comparison between the obtained simulation results and experimental data taken from Huang et al. [20] and corresponding to body temperature of 25°C.

Figure 9 shows that the obtained results in terms of force-displacement curves show a close agreement between numerical perditions and experimental results, revealing that the proposed model captures the essential behavior of SMA helical springs with regards to SE effect as observed during experiment. There are, however, some variations existing between the experimental and finite element simulation results. They are probably due to the fact that the material property α was not evaluated experimentally; in fact, it was identified here to yield the least discrepancies between simulation and experimental data. Besides, the implemented version of Auricchio model in ANSYS works with an averaged Young's modulus for both martensite and austenite domains, while these modules are in general different as pointed out by the experimental data given in [20] and recalled in Table 1.

3.1.2. *Influence of temperature on the SMA helical spring response.* Simulation of the SMA helical spring response in terms of force-displacement curve was also performed by varying body temperature and amplitude of displacement according to Table 5.

Figure 10 illustrates the effect of body temperature on the helical spring reaction.

To analyze in more detail the effect of temperature on helical spring behavior, the following quantities were calculated: maximum reaction force, average (secant) stiffness at loading and total damping energy. Table 6 summarizes the obtained response characteristics of helical spring as function of the combination number.

For all cases, the initial tangent stiffness at loading was constant and does not depend on body temperature. Its value is $K_i = 114\ N.m^{-1}$. Table 6 shows that the secant stiffness increases with body temperature, and that the maximum reaction force and total damping energy increase with both displacement amplitude and body temperature. At lower temperatures, the stiffness is lower and the hysteresis area is larger. On the other hand, at higher temperatures, the average stiffness is increased while the hysteresis area decreases.

To get deeper comprehension of stiffness dependency on temperature, let us recall a classical analytical relationship which links the SMA helical spring response to its body temperature, according to linear theory of helical springs. The average stiffness can be estimated as:

$$K_m = \frac{G r_0^2}{16 N R_0^3} \tag{6}$$

where G is the material shear modulus.

It is well known that for a NiTi based SMA, G increases with temperature dissimilar to other metallic materials.

To be able to quantify the influence of temperature on helical spring response, explicit response surface models based on nonlinear regression of the results given in Table 6 were derived. The obtained models for the maximum

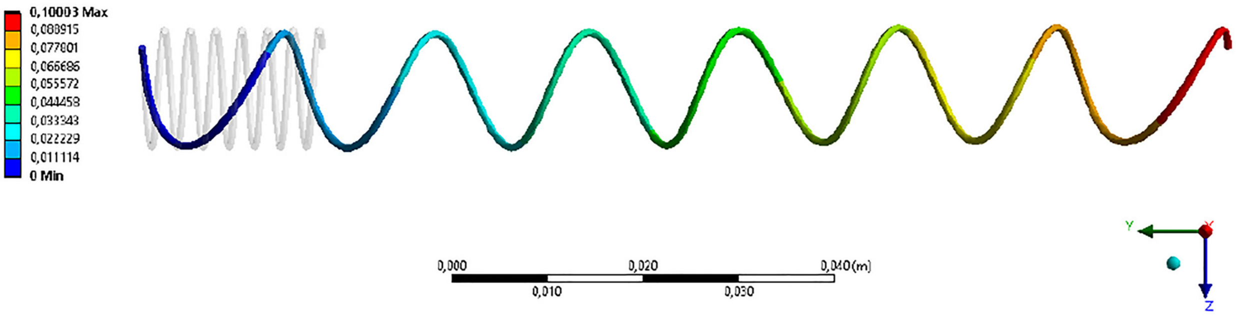

Fig. 8. SMA helical spring, initial and deformed configurations under 100mm maximum displacement

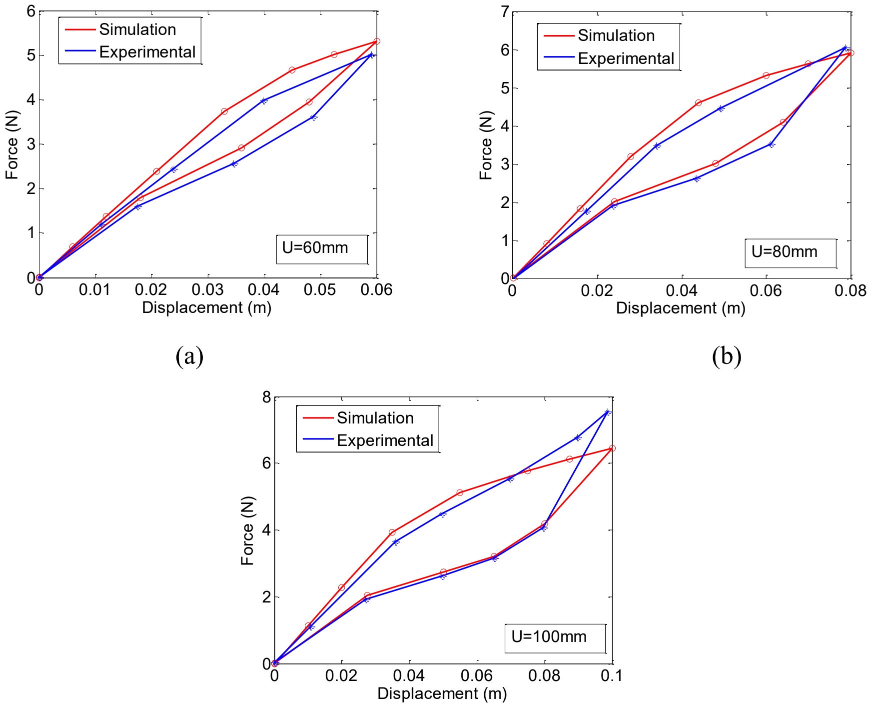

(a)

(b)

(c)

Fig. 9. Comparison of numerical force-displacement curves and experimental data [20] for a cycle loading-unloading of the SMA helical spring and three imposed displacement amplitudes U

reaction load, average stiffness and total damping energy have the following quadratic polynomials forms:

$$F_{\max} = 1.324 + 37.73U + 0.06967T + 0.3875UT - 112.5U^2 - 0.00035T^2 \tag{7}$$

$$K_m = 1111 - 1304U + 2.007T - 8.5UT + 5833U^2 - 0.00517T^2 \tag{8}$$

$$D_m = 0.4398 - 12.54U + 0.003267T + 0.1725UT + 102.1U^2 - 0.0001617T^2 \tag{9}$$

Regressions defined by equations (7), (8) and (9) were obtained with a high value of the coefficient of determination R^2, which reaches respectively 99.9%, 100% and 97.9%. So they can reliably be used in sizing helical springs, as long as body temperature and applied amplitude cycle of displacement remain in their respective considered ranges here: $T \in [15, 35]\ (^\circ C)$ and $U \in [0.06, 0.1]\ (m)$.

Analysis of variance performed on the results given in Table 6 has shown that for the maximum reaction force, temperature T is dominant with 66%, the amplitude U has a participation of 33% while the interaction between U and T is negligible. For the average stiffness, almost equal influence of temperature and amplitude is observed with respectively 45% and 54% for each one of them, while their interaction remains negligible. As for the total damping energy, the amplitude of displacement is dominant with up to 73% and temperature represents 22% of variability source, while again only negligible interaction between these two factors is observed.

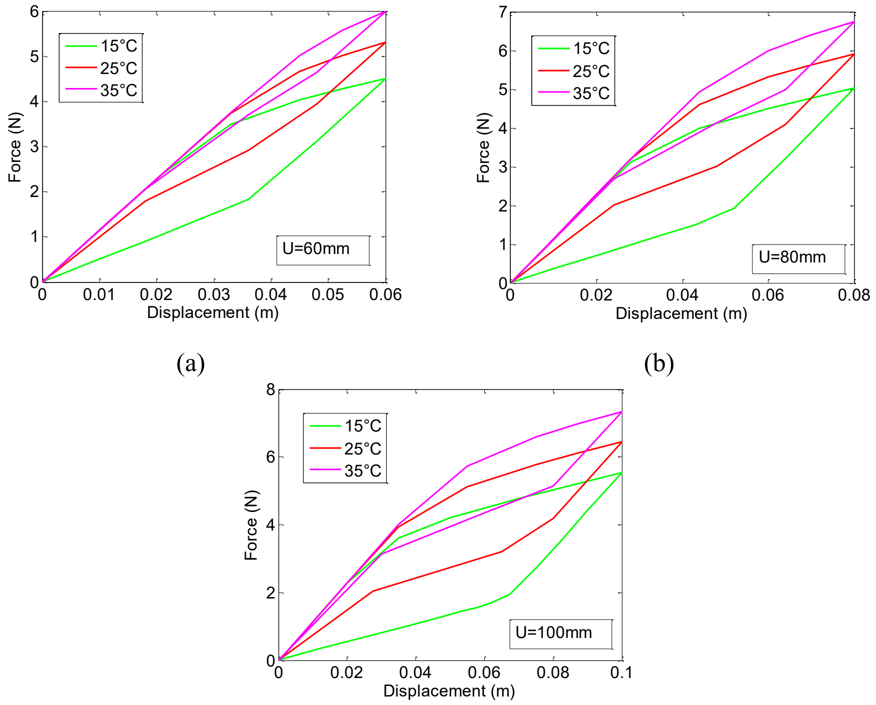

(a) (b)

(c)

Fig. 10. Force-displacement curves of the SMA helical spring as function of imposed amplitude of a cycle of displacement and body temperature

3.2. Simulation of one-way SME in SMA helical springs

In this section, results of one-way SME simulations are presented. These were performed for helical spring having the geometries defined in Table 4, and for which the material characteristics are those given in Table 2. Nine different 3D geometries of SMA helical springs were elaborated under ANSYS CAE interface, before calculating through static structural analysis and the option SME the response of each spring under the thermomechanical loading given in Fig. 4.

Table 7 shows the obtained results in terms of weight of springs, strain energy and maximum force.

Table 6. Response characteristics of helical spring as function of the combination number

Combination number	Maximum reaction force $F_{\max}(N)$	Secant stiffness at loading K_m $(N.m^{-1})$	Total damping energy E_d (J)
1	4.50	75.0	0.243
2	5.31	88.5	0.288
3	5.98	99.7	0.320
4	5.03	62.9	0.265
5	5.91	73.9	0.438
6	6.75	84.4	0.512
7	5.54	55.4	0.503
8	6.45	64.5	0.603
9	7.33	73.3	0.718

Table 7. ANSYS output response characteristics of simulated helical springs under one-way SME

Case number	Weight (mkg)	Strain energy (μJ)	Maximum force (N)
1	0.1911	0.1240	0.2732
2	0.1898	0.1864	0.2653
3	0.1887	0.2761	0.2677
4	0.1949	0.2163	0.2554
5	0.1935	0.1838	0.2564
6	0.1924	0.1831	0.2572
7	0.2061	0.1841	0.2259
8	0.2047	0.1878	0.2373
9	0.2035	0.1879	0.2379

Figure 11 gives the force-displacement curves of all the considered helical springs when they are submitted to the one-way thermomechanical loading as defined in Fig. 4.

Analysis of variation of the obtained results given in Table 7 indicates that for the considered ranges of factors, helical spring radius has a dominant influence on mass with 97.3% and length has only a small influence with 2.7%. As to the maximum force variability, it is mainly explained by the radius 93.6%, which is followed by the interaction of radius with length 5.5% and finally length which participates by only 0.5%.

From the results given in Table 7, one can derive quadratic polynomial regressions of mass and maximum force as function of helical spring radius and length under the following forms:

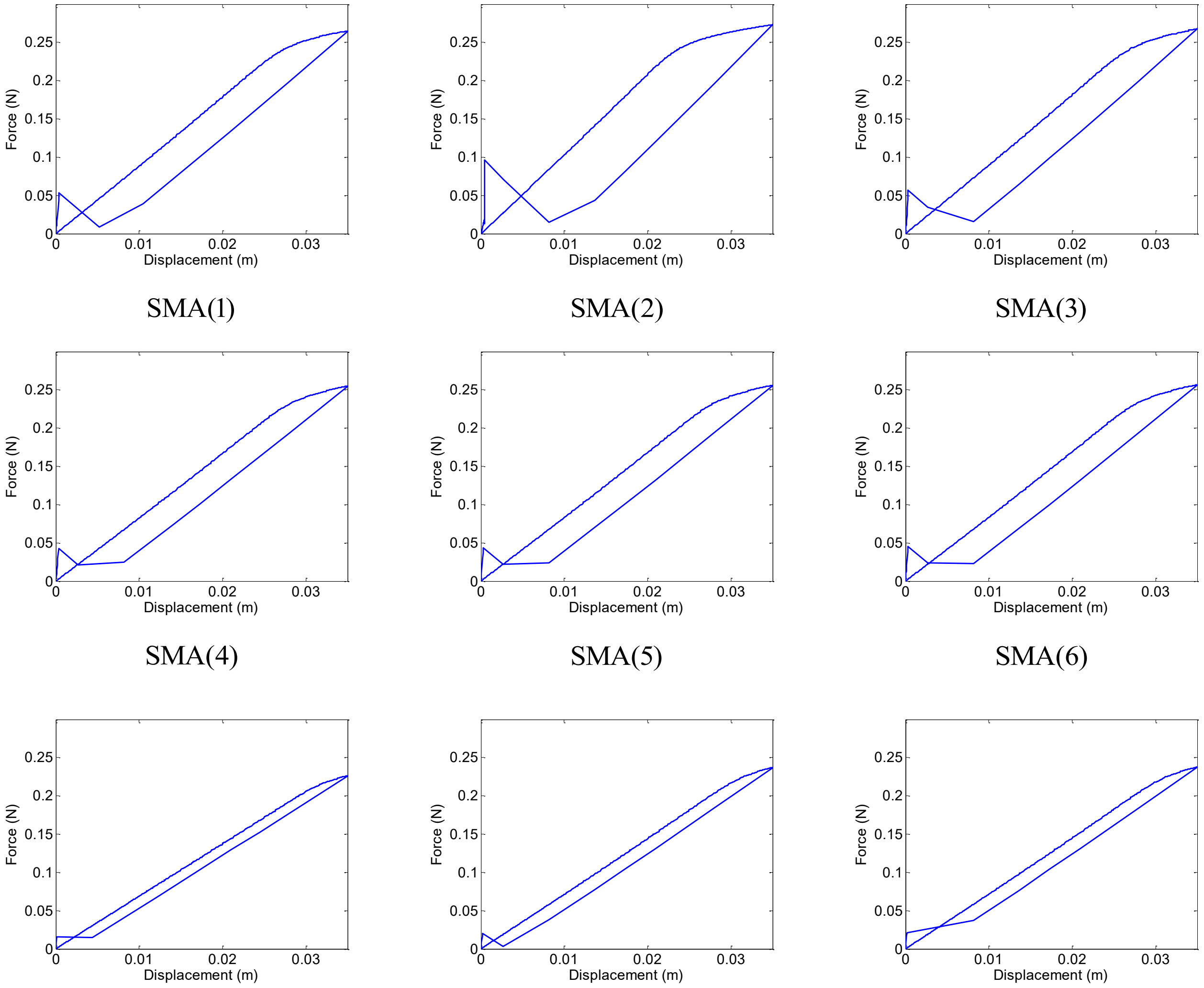

SMA(1) SMA(2) SMA(3)

SMA(4) SMA(5) SMA(6)

SMA(7) SMA(8) SMA(9)

Fig. 11. One-way SME force-displacement curves for helical springs defined in Table 4 under the action of thermomechanical loading given in Fig. 4

$$\begin{aligned}\text{Mass} =& 1.277 - 0.4195R_0 - 0.001283L_0 - 8.333\\ &\times 10^{-5}R_0L_0 + 0.04130R_0^2 + 2.917\times 10^{-5}L_0^2\end{aligned} \tag{10}$$

$$\begin{aligned}F_{\max} =& -0.3616 + 0.4171R_0 - 0.03757L_0\\ &+ 0.007292R_0L_0 - 0.05685R_0^2 - 2.917\times 10^{-5}L_0^2\end{aligned} \tag{11}$$

The associated coefficient of determination is respectively $R^2 = 100\%$ and $R^2 = 98\%$. This states that the previous polynomial regressions can be reliability used for sizing helical springs in the considered ranges of factors: $R_0 \in [5.1, 5.7]$ (mm) and $L_0 \in [17, 21]$ (mm). In particular, they can be used in the framework of a multi-objective optimization problem aiming at minimizing both Mass and $F_{\max}$, while maximizing the helical spring course.

4. CONCLUSIONS

In this work, focus was on establishing force-displacement curves of nickel-titanium shape memory alloy based helical spring, for both superelasticity effect and one-way shape memory effect, by using the finite element method under ANSYS software packages. These curves were derived in a systematic way which can contribute to ease the procedure of design of helical springs. At first, comparison between numerical predictions and experimental data has been performed to assess convergence of the finite element method. Then, a parametric study was conducted to analyze the influence of temperature on the superelastic spring response. Explicit correlations were obtained. They corroborate in particular the classical shape memory alloys behavior where the increase of temperature causes higher stiffness and low hysteresis. Considering the one-way shape memory effect which has received small interest in the field of numerical computation, simulations were conducted and enabled to assess dependency of the response on key geometrical parameters. The obtained results have emphasized the alternative of using a simulation based methodology in order to achieve improved design of helical springs made of shape memory alloys.

REFERENCES

[1] L. C. Brinson, “One-dimensional constitutive behavior of shape memory alloys: thermomechanical derivation with non-constant material functions and redefined martensite internal variable,” *J. Intell. Mater. Syst. Structures*, vol. 4, no. 2, pp. 229–42, 1993. https://doi.org/10.1177/1045389X9300400213.

[2] Y. Toi, J.B. Lee, and M. Taya, “Magneto-superelastic analysis of shape memory alloy helical spring actuators controlled by magnetic force,” *J. Comput. Sci. Technol.*, vol. 2, no. 1, pp. 11–22, 2008. https://doi.org/10.1299/jcst.2.11.

[3] S. Alazzawi, and P. Filip, “Modeling the transient behavior of the NiTi shape memory actuator using finite element analysis: parametric study of the rate effects,” *Results Mater.*, vol. 1, p. 100015, 2019. https://doi.org/10.1016/j.rinma.2019.100015.

[4] J. Uchil, K.G. Kumara, and K.K. Mahesh, “Effect of thermal cycling on R-phase stability in a NiTi shape memory alloy,” *Mater. Sci. Eng. A*, vol. 332, nos 1–2, pp. 25–8, 2002. https://doi:10.1016/s0921-5093(01)01711-7.

[5] F. Auricchio, R.L. Taylor, and J. Lubliner, “Shape-memory alloys: macromodelling and numerical simulations of the superelastic behavior,” *Comput. Methods Appl. Mech. Eng.*, vol. 146, nos 3–4, pp. 281–312, 1997. https://doi.org/10.1016/S0045-7825(96)01232-7.

[6] E. McCummiskey, W.M. Dempster, D.H. Nash, T.R. Ashton, and D.G. Stevenson, “The determination and evaluation of Nitinol constitutive models for finite element analysis,” *Appl. Mech. Mater.*, vols 7–8, pp. 81–8, 2007. https://doi.org/10.4028/www.scientific.net/AMM.7-8.81.

[7] F. Auricchio and R.L. Taylor, “Shape-memory alloys: modelling and numerical simulations of the finite-strain superelastic behavior,” *Comput. Methods Appl. Mech. Eng.*, vol. 143, nos 1–2, pp. 175–94, 1997. https://doi.org/10.1016/S0045-7825(96)01147-4.

[8] F. Auricchio and L. Petrini, “Improvements and algorithmical considerations on a recent three dimensional model describing stress induced solid phase transformations,” *Int. J. Numer. Methods Eng.*, vol. 55, no. 11, pp. 1255–84, 2002. https://doi.org/10.1002/nme.619.

[9] F. Auricchio, “Robust integration-algorithm for a finite-strain shape-memory-alloy,” *Int. J. Plasticity*, vol. 17, no. 7, pp. 971–90, 2001. https://doi.org/10.1016/S0749-6419(00)00050-4.

[10] A.C. Souza, E.N. Mamiya, and N. Zouain, “Three-dimensional model for solids undergoing stress-induced phase transformations,” *Eur. J. Mech. - A/Solids*, vol. 17, no. 5, pp. 789–806, 1998. https://doi.org/10.1016/S0997-7538(98)80005-3.

[11] J.M.B Sobrinho, F.M.F. Filho, A. Emiliavа, M.F. Cunha, C.R. Souto, S.A. Silva, and A. Ries, “Experimental and numerical analyses of a rotary motor using shape memory alloy mini springs,” *Sensors Actuators A: Phys.*, vol. 302, no. 1, p. 111823, 2020. https://doi.org/10.1016/j.sna.2019.111823.

[12] A. Concilio, V. Antonucci, F. Auricchio, L. Lecce, and E. Sacco, *Shape Memory Alloy Engineering for Aerospace, Structural, and Biomedical Applications*, 2nd Edition. Butterworth-Heinemann, 2021. https://doi.org/10.1016/C2018-0-02430-5.

[13] N.V. Viet, W. Zaki, R. Umer, and C. Cissé, “Analytical model for the torsional response of superelastic shape memory alloy circular sections subjected to a loading-unloading cycle,” *Int. J. Sol. Structures*, vols 156–157, pp. 49–60, 2019. https://doi.org/10.1016/j.ijsolstr.2018.08.001.

[14] N.V. Viet, W. Zaki, R. Umer, and Y. Xu, “Mathematical model for superelastic shape memory alloy springs with large spring index,” *Int. J. Sol. Structures*, vols 185–186, pp. 159–69, 2020. https://doi.org/10.1016/j.ijsolstr.2019.08.022.

[15] L. Esposito, M. Fraldi, E. Ruocco, and E. Sacco, “A shape memory alloy helix model accounting for extension and torsion,” *Eur. J. Mech. - A/Solids*, vol. 89, p. 104281, 2021. https://doi.org/10.1016/j.euromechsol.2021.104281.

[16] S. Moaveni, *Finite Element Analysis, Theory and Application with ANSYS*. Croydon, UK: Pearson Education Limited, CPI Group Ltd, 2015, ISBN 10: 0-273-77430-1.

[17] P. Kohnke, *ANSYS Mechanical APDL Theory Reference*, ANSYS, Inc. Release 15.0. Canonsburg, PA, USA: Southpointe, 2013.

[18] S. Ahmad, B.M. Irons, and O.C. Zienkiewicz, *Theory Reference for the Mechanical APDL and Mechanical Applications 1226*. 2009.

[19] G. Maîtrejean, P. Terriault, D. Devís Capilla, and V. Brailovski, “Unit cell analysis of the superelastic behavior of open-cell tetrakaidecahedral shape memory alloy foam under quasi-static loading,” *Smart Mater. Res.*, vol. 2014, 2014, Paper no. 870649 https://doi.org/10.1155/2014/870649.

[20] B. Huang, Lv. Hongwang, and Y. Song, “Numerical simulation and experimental study of a simplified force-displacement relationship in superelastic SMA helical springs,” *Sensors*, vol. 19, no. 1, p. 50, 2019. https://doi.org/10.3390/s19010050.

[21] H. Khodaei, *Modeling of Bulk and Porous Shape Memory Alloys*, Doctoral Dissertation, Canada, Ecole de Technologie Supérieure, Université du Québec, 2020.

[22] A. Gautam, M.A. Callejas, A. Acharyya, and S.G. Acharyya, “Shape-memory-alloy-based smart knee spacer for total knee arthroplasty: 3D CAD modelling and a computational study,” *Med. Eng. Phys.*, vol. 55, pp. 43–51, 2018. https://doi.org/10.1016/j.medengphy.2018.03.001.

[23] P.C.S. Da Silva, C.J. De Araujo, M.A. Savi, and N.C. Santos, “Simulation of the superelastic behavior of Ni-Ti Belleville washers using ANSYS,” *22nd International Congress of Mechanical Engineering (COBEM 2013)*, November 3-7, Ribeirao Preto, Brazil, 2013.

APPENDIX A

Auricchio SMA material behavior under SE deformation

To characterize superelastic behavior of a SMA, Auricchio’s model considers three-phase transformations: austenite to single-variant martensite ($A \rightarrow S$), single-variant martensite to austenite ($S \rightarrow A$), and reorientation of the single-variant martensite ($S \rightarrow S$). Assuming the material to be perfectly isotropic, only two phases are considered: the austenite (A) and the single-variant martensite (S).

Two internal variables are introduced: martensite volume fraction ξ_S and austenite volume fraction ξ_A. These two variables satisfy the following relation:

$$\xi_S + \xi_A = 1 \tag{A1}$$

So, only one independent internal variable holds; the martensite volume fraction ξ_S is chosen in the following as the independent internal variable.

In order to model the pressure dependency of the phase transformation, Drucker-Prager loading function is used. This takes the following form:

$$F = q + 3\alpha p \tag{A2}$$

with

$$q = \sqrt{\frac{3}{2}\overline{\overline{s}} : \overline{\overline{s}}} \text{ and } p = \frac{1}{3} tr(\overline{\overline{\sigma}}) \tag{A3}$$

where α is a material parameter, $\overline{\overline{s}} = \overline{\overline{\sigma}} - p\overline{\overline{1}}$ is the deviatoric stress tensor and tr the trace operator.

The evolution of the martensite volume fraction is expressed as follows:

$$\dot{\xi}_S = \begin{cases} -H^{AS}(1-\xi_S)\dfrac{\dot{F}}{F - R_f^{AS}} & A \rightarrow S \text{ transformation} \\[2ex] -H^{SA}\xi_S\dfrac{\dot{F}}{F - R_f^{SA}} & S \rightarrow A \text{ transformation} \end{cases} \tag{A4}$$

The H parameters are scalar quantities and they are defined by the following relations:

$$H^{AS} = \begin{cases} 1 & if \quad R_s^{AS} < F < R_f^{AS} \text{ and } \dot{F} > 0 \\ 0 & \text{otherwise} \end{cases} \tag{A5}$$

$$H^{SA} = \begin{cases} 1 & if \quad R_f^{SA} < F < R_s^{SA} \text{ and } \dot{F} < 0 \\ 0 & \text{otherwise} \end{cases} \tag{A6}$$

with

$$\begin{cases} R_s^{AS} = \sigma_s^{AS}(1+\alpha) \\ R_f^{AS} = \sigma_f^{AS}(1+\alpha) \\ R_s^{AS} = \sigma_s^{SA}(1+\alpha) \\ R_f^{SA} = \sigma_f^{SA}(1+\alpha) \end{cases} \tag{A7}$$

where $\sigma_s^{AS} = \sigma_{Ms}$, $\sigma_f^{AS} = \sigma_{Mf}$, $\sigma_s^{SA} = \sigma_{As}$ and $\sigma_f^{SA} = \sigma_{Af}$ are the critical stresses at the start of martensite, finish of martensite, start of austenite, and finish of austenite transformation respectively. They are shown in Fig. A1.

The parameter α characterizes the tension-compression asymmetry. In the case for which tensile and compressive behavior are symmetrical, $\alpha = 0$ holds. Otherwise, if the tension and compression states are uniaxial, the parameter α can be linked with the initial value of austenite to martensite phase transformation in tension σ_t^{AS} and compression σ_c^{AS} respectively as [23]:

$$\alpha = \frac{\sigma_c^{AS} - \sigma_t^{AS}}{\sigma_c^{AS} + \sigma_t^{AS}} \tag{A8}$$

The constitutive relation for Auricchio's model is given by the following equations:

$$\ddot{\widehat{\overline{\overline{\tau}}}} = \overline{\overline{\overline{\overline{D}}}} : \left(\ddot{\widehat{\overline{\overline{\varepsilon}}}} - \ddot{\widehat{\overline{\overline{\varepsilon}}}}_{tr} \right) \tag{A9}$$

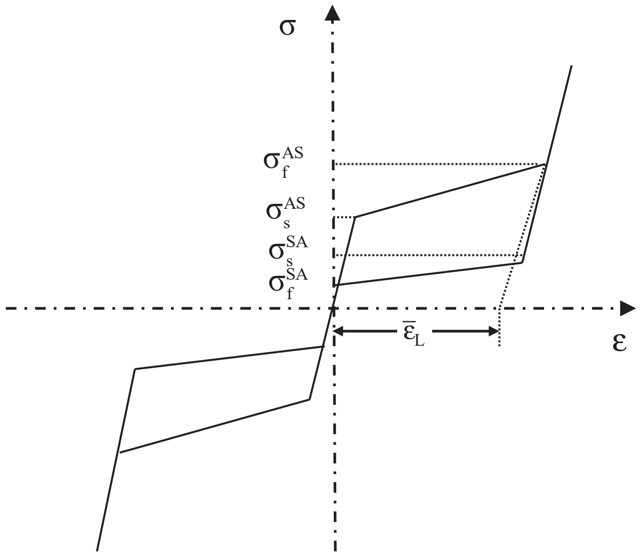

Fig. A1. Idealized one-dimensional stress-strain diagram for superelastic behavior of SMA according to Auricchio model

$$\ddot{\widehat{\overline{\overline{\varepsilon}}}}_{tr} = \dot{\xi}_S \overline{\varepsilon}_L \frac{\partial F}{\partial \overline{\overline{\sigma}}} \tag{A10}$$

where $\overline{\overline{\tau}}$ and $\overline{\overline{\varepsilon}}$ are Kirchhoff stress and left Cauchy-Green strain respectively, $\overline{\overline{\overline{\overline{D}}}}$ is the tangent elastic stiffness tensor of SMA material [7], $\overline{\overline{\varepsilon}}_{tr}$ is the transformation strain tensor, $\overline{\varepsilon}_L$ represents the material parameter associated with maximum recoverable strain, see Fig. A1, and F is the Drucker-Prager like loading function which is defined in Eq. (A2).

The material parameters for the superelastic SMA model consist then of the six following constants:

- σ_s^{AS} the starting stress value for the forward austenite-martensite phase transformation;
- σ_f^{AS} the final stress value for the forward austenite-martensite phase transformation;
- σ_s^{SA} the starting stress value for the reverse martensite-austenite phase transformation;
- σ_f^{AS} the final stress value for the reverse martensite-austenite phase transformation;
- $\overline{\varepsilon}_L$ the maximum transformation shear strain;
- α the parameter measuring the difference between material responses in tension and compression.

APPENDIX B

Auricchio SMA material behavior under SME deformation

For SME simulation, a three-dimensional thermomechanical model for stress-induced solid phase transformations was developed by Auricchio and Petrini [8]. This model was recognized to be efficient and able to reproduce all of the key characteristics of SMA in a 3D setting. In this modeling, the free energy is set as follows:

$$\psi\left(\theta,\ \overline{\overline{e}},\ T,\ \overline{\overline{\varepsilon}}_{tr}\right)=\frac{1}{2}(\overline{\overline{\varepsilon}}-\overline{\overline{\varepsilon}}_{tr}):\overline{\overline{\overline{\overline{D}}}}:(\overline{\overline{\varepsilon}}-\overline{\overline{\varepsilon}}_{tr})+\tau_M(T)\left\|\overline{\overline{e}}_{tr}\right\|+\frac{h}{2}\left\|\overline{\overline{e}}_{tr}\right\|^2+1_{\overline{\overline{\varepsilon}}_{tr}}\left(\overline{\overline{e}}_{tr}\right) \quad \text{(B1)}$$

WHERE $\overline{\overline{\varepsilon}}$, $\overline{\overline{e}}$, $\overline{\overline{\varepsilon}}_{tr}$, $\overline{\overline{e}}_{tr}$ are respectively total strain tensor, total deviatoric strain tensor, transformation strain tensor and deviatoric transformation strain tensor, θ is the volumetric strain, $\overline{\overline{\overline{\overline{D}}}}$ is the elastic stiffness of SMA material; T the ambient temperature, $\tau_M(T)=\langle\beta(T-T_0)\rangle^+$ is a positive and monotonically increasing function of the temperature in which $\langle\cdot\rangle^+$ is the positive part of the argument, β a material parameter and T_0 the temperature below which no twinned martensite is observed; $\|\cdot\|$ is the Euclidean norm; h is a material parameter related to the hardening of the material during the phase transformation. Finally, $1_{\overline{\overline{\varepsilon}}_{tr}}\left(\overline{\overline{e}}_{tr}\right)$ is an indicator function introduced to satisfy the constraint on the transformation strain norm and it is given by the following equation:

$$1_{\overline{\overline{\varepsilon}}_{tr}}\left(\overline{\overline{e}}_{tr}\right)=\begin{cases}0 & if\ 0\le\left\|\overline{\overline{e}}_{tr}\right\|\le\overline{\varepsilon}_L\\ +\infty & \text{otherwise}\end{cases} \quad \text{(B2)}$$

Accordingly, one can write:

$$\overline{\overline{\sigma}}=\frac{\partial\psi}{\partial\overline{\overline{\varepsilon}}}=\overline{\overline{\overline{\overline{D}}}}:(\overline{\overline{\varepsilon}}-\overline{\overline{\varepsilon}}_{tr}) \quad \text{(B3)}$$

$$\overline{\overline{X}}_{tr}=-\frac{\partial\psi}{\partial\overline{\overline{e}}_{tr}} \quad \text{(B4)}$$

where $\overline{\overline{X}}_{tr}$ represents the transformation stress tensor.

Splitting the strain tensor $\overline{\overline{\varepsilon}}$ and the stress tensor $\overline{\overline{\sigma}}$, one obtains:

$$\overline{\overline{\varepsilon}}=\overline{\overline{e}}+\frac{1}{3}\theta\overline{\overline{1}} \quad \text{(B5)}$$

$$\overline{\overline{\sigma}}=\overline{\overline{s}}+p\overline{\overline{1}} \quad \text{(B6)}$$

where $\overline{\overline{s}}$ is the deviatoric stress, p is the main or hydrostatic stress and $\overline{\overline{1}}$ is the unit tensor.

Equation (B4) can be rewritten as:

$$\overline{\overline{X}}_{tr}=\overline{\overline{s}}-\frac{1}{\left\|\overline{\overline{e}}_{tr}\right\|}\left[\tau_M(T)+h\left\|\overline{\overline{e}}_{tr}\right\|+\gamma\right]\overline{\overline{e}}_{tr} \quad \text{(B7)}$$

with γ is defined as:

$$\gamma=\begin{cases}0 & if\ 0\le\left\|\overline{\overline{e}}_{tr}\right\|\le\overline{\varepsilon}_L\\ \ge 0 & \left\|\overline{\overline{e}}_{tr}\right\|=\overline{\varepsilon}_L\end{cases} \quad \text{(B8)}$$

where $\overline{\varepsilon}_L$ represents the maximum transformation strain.

To catch the asymmetric behavior observed on SMA materials during tension–compression test, Auricchio and Petrini [8] have proposed a Prager-Lode type limit function which depends on the second J_2, and the third J_3 stress deviator invariants of the transformation under the following form:

$$F(\overline{\overline{X}}_{tr})=\sqrt{2J_2}+m\frac{J_3}{J_2}-R \quad \text{(B9)}$$

where m is a material parameter describing Lode dependency and R is the elastic limit. J_2 and J_3 are defined in the following way:

$$J_2=\frac{1}{2}\overline{\overline{X}}_{tr}^{2}:\overline{\overline{1}} \quad \text{(B10)}$$

$$J_3=\frac{1}{2}\overline{\overline{X}}_{tr}^{3}:\overline{\overline{1}} \quad \text{(B11)}$$

The evolutionary equations of strain transformation are defined as:

$$\begin{cases}\dot{\overline{\overline{\varepsilon}}}_{tr}=\dot{\xi}\overline{\varepsilon}_L\frac{\partial F}{\partial\overline{\overline{\sigma}}} \qquad \dot{\xi}\ge 0 \qquad \dot{\xi}\ F\left(\overline{\overline{X}}_{tr}\right)=0\end{cases} \quad \text{(B12)}$$

where ξ is an internal variable, called the transformation strain multiplier. The second and third relations of Equation (B12) are the Kuhn–Tucker conditions, which reduces the problem to a constrained optimization problem.

The SME effect option is like this described by six constants: h, T_0, R, β, $\overline{\varepsilon}_L$, m in addition to the martensite modulus E_m and Poisson's ratio ν. These constants define the stress-strain behavior of material in loading and unloading cycles for the uniaxial stress-state and thermal loading.